Atomic structure of surface defects in alumina studied by dynamic force microscopy: strain-relief-, translation- and reflection-related boundaries, including their junctions

2011 New J. Phys. 13 123028

(http://iopscience.iop.org/1367-2630/13/12/123028)

New Journal of Physics
The open-access journal for physics

Atomic structure of surface defects in alumina studied by dynamic force microscopy: strain-relief-, translation- and reflection-related boundaries, including their junctions

G H Simon, T König, L Heinke, L Lichtenstein, M Heyde[1] and H-J Freund

Fritz-Haber-Institut der Max-Planck-Gesellschaft, Faradayweg 4-6, D-14195 Berlin, Germany
E-mail: heyde@fhi-berlin.mpg.de

New Journal of Physics **13** (2011) 123028 (21pp)
Received 16 August 2011
Published 21 December 2011
Online at http://www.njp.org/
doi:10.1088/1367-2630/13/12/123028

Abstract. We present an extensive atomic resolution frequency modulation dynamic force microscopy study of ultrathin aluminium oxide on a single crystalline NiAl(110) surface. One-dimensional surface defects produced by domain boundaries have been resolved. Images are presented for reflection domain boundaries (RDBs), four different types of antiphase domain boundaries, a nucleation-related translation domain boundary and also domain boundary junctions. New structures and aspects of the boundaries and their network are revealed and merged into a comprehensive picture of the defect arrangements. The alumina film also covers the substrate completely at the boundaries and their junctions and follows the structural building principles found in its unit cell. This encompasses square and rectangular groups of surface oxygen sites. The observed structural elements can be related to the electronic signature of the boundaries and therefore to the electronic defects associated with the boundaries. A coincidence site lattice predicted for the RDBs is in good agreement with experimental data. With $\Sigma = 19$ it can be considered to be of low-sigma

[1] Author to whom any correspondence should be addressed.

type, which frequently coincides with special boundary properties. Images of asymmetric RDBs show points of good contact alternating with regions of nearly amorphous disorder in the oxygen sublattice.

Contents

1. Introduction

Frequency modulation dynamic force microscopy (FM-DFM) is capable of resolving complex surface structures and their defects on electrically conductive and insulating crystalline or amorphous materials. It achieves a surface sensitivity that may exceed that of scanning tunnelling microscopy (STM), especially when it comes to metal-supported thin films such as the ultrathin alumina on NiAl(110) studied in this work. Linear and planar defects are prominent ingredients of crystalline materials and may form networks therein. They deserve attention as they substantially affect properties such as diffusion, electrical conductivity, dielectric breakdown, elastic behaviour and phase transitions. Their intersections with the surface may act as material sink or source through transport, but also influence growth and chemical reactivity, which renders them of interest for the fields of surface chemistry and heterogeneous catalysis. While dubbed *defects*, they are not always undesirable, such as in work hardening of metals, in the growth of whiskers and in defect-engineered novel materials and devices [1, 2]. The structure and properties of such defects are intimately related to the symmetry and chemical properties of the host material. Since many questions regarding the structural chemistry, especially of oxides and their meta-stable polymorphs, remain unanswered, it is not surprising that defect characterization of, for example, aluminium oxide phases is still an active subject. Defects as found in domain boundaries could be used as an experimental analogy to the artificial lattice modifications employed by theorists, and may help one to gain a deeper understanding of the unperturbed materials such as meta-stable bulk alumina phases.

In epitaxial systems, defects are inevitable—be it the phase boundary to the epilayer or dislocations and domain boundaries formed as a consequence of the differences between the adjacent lattices. The ultrathin ordered aluminium oxide overlayer on NiAl(110) is therefore known not only for its simple and reliable preparation and smooth coverage of the metal substrate, but also for its rich and reproducible defect network. Alumina/NiAl(110) is a result of modelling efforts in corrosion science and for catalyst supports in model catalysis [3–5].

It has been successfully used in studies on the initial steps of nucleation and the charging of adsorbates [6, 7]. It is used to model, among other things, automotive NO_x storage catalysts [8] and ionic liquid catalysts [9]. It has been used as a decoupling layer in experiments on single-atom magnetism [10] as well as single-molecule fluorescence and vibrational spectroscopy [11, 12]. In the course of these works, it has been recognized repeatedly that the defect network induces characteristic alterations in chemical and physical properties such as reactivity, work function as well as adsorption and nucleation [13–17]. However, the lack of knowledge about defect structures limits atomic scale studies on this film system. Recently, it was acknowledged that the film belongs to a class of two-dimensional (2D) alumina films with similar if not identical structures on Cu-9%Al(111), FeAl(110), Ag(111), Ni(111), Ni_3Al(111) and aluminium-containing quasi-crystals [18–24]. They represent a class of possible candidates for passivation studies or applications in microelectromechanical systems, corrosion and fabrication of magnetic, electronic or optical devices. It has also to be clarified to what extent its surface reconstruction resembles that of meta-stable alumina polymorphs, in particular when they are highly dispersed and one can speculate whether other sesquioxides form equivalent oxide films on corresponding substrates.

In this paper, we present a comprehensive atomic resolution dynamic force microscopy study of several new as well as known surface structures of the defect network. In particular, structures of all three classes of strain-relief, translation- and point-symmetry-related domain boundaries as well as junctions between them are presented for the first time alongside and in connection with one another. Structural complexity increases as we proceed and FM-DFM reveals nearly amorphous disorder within the oxygen sublattice at the reflection domain boundaries (RDBs), highlighting another virtue of this local probe. Figure 1 shows the epitaxial relation between the film and the substrate, a schematic diagram of the different domain boundary classes and an image of the oxide film on two neighbouring terraces giving an idea of the various boundary types. Alumina/NiAl(110) grows in a smooth 2D fashion with step edges induced solely by the substrate. Its strain-relief-related translation domain boundaries (TDBs) are known as antiphase domain boundaries (APDBs) [15, 25]. Nucleation- and growth-related TDBs formed by impinging crystalline patches exist as well, but show different behaviour. Reflection domain boundaries (RDBs) result from the different point symmetries in the film and the substrate. Atomic structures of the latter two classes are shown for the first time. Nucleation-related TDBs and RDBs delimit more or less compact oxide patches due to their relation to nucleation and growth. APDBs, in turn, are produced within such an oxide patch [15] at high areal density and form domains with a high length-to-width ratio (sometimes more than 10). They also form networks in such an oxide patch.

A description of the domain boundaries as line defects has been adopted in previous works due to their 1D appearance in scanning probe microscopy (SPM). A more sophisticated picture links them to dislocations which terminate the stacking fault at the film–substrate interface along NiAl[$1\bar{1}0$] [15]. With the alumina/NiAl(110) film thickness in the range of dislocation core diameters, the displacement across the boundary is considered to be equal to the Burgers vectors of the underlying misfit dislocations. The domain boundary network is therefore identified with a dislocation network at the film–substrate interface and to be basically 2D. The glide plane of the dislocations is the film–substrate interface.

FM-DFM provides a contrast that maps the surface oxygen (O_S) sites of the alumina/NiAl(110) structure as protrusions [20].

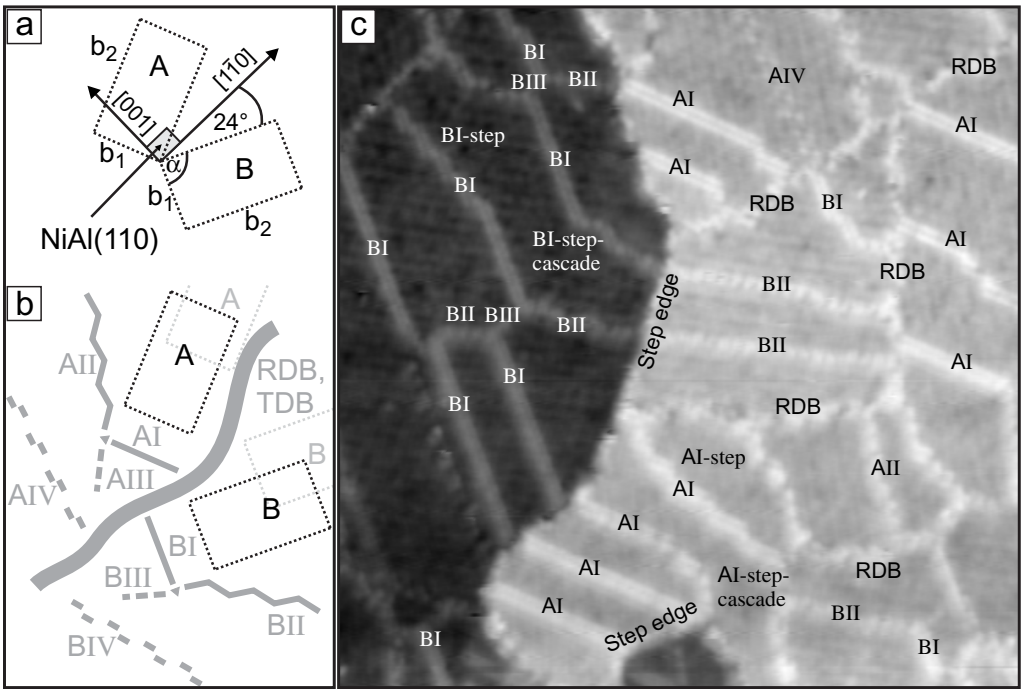

Figure 1. Domain boundary network of ultrathin alumina on NiAl(110). (a) Diagram of the geometry and relation between the unit cells ($b_1 = 10.55$ Å, $b_2 = 17.88$ Å, $\alpha = 88.7°$, rotation against NiAl[1$\bar{1}$0]: $\pm 24°$) of the two oxide reflection domains and the relation to their NiAl(110) substrate (4.08 Å × 2.89 Å). (b) Orientation of the translation- and reflection-related domain boundaries with respect to the oxide lattice. (c) STM image of various domain boundaries protruding at the applied tunnelling parameters as bright lines on two adjacent terraces of ultrathin alumina on NiAl(110). Symbols mark a step edge, RDBs, APDBs of different types (I–IV) and steps and step-cascades in type I APDBs. Sample bias voltage $V_S = +3.5$ V, tunnelling current $I_T = +400$ pA; scan area: 100 nm × 100 nm.

2. Experimental details

All data have been recorded in ultrahigh vacuum (UHV) at cryogenic temperature (5 K). The microscope used is a custom built dual-mode FM-DFM/STM [26] situated in a helium bath cryostat. The implemented force microscopy method is also known as non-contact atomic force microscopy (NC-AFM). The microscope is equipped with a quartz tuning fork sensor which comprises a Pt/Ir wire attached with electrically insulating epoxy adhesive to one quartz prong as a tip. With the use of an electrically separate tunnelling current wire, special attention has been paid to the separation of the tunnelling current from force sensing via the tuning fork electrodes [27, 28]. Equally important is the prevention of saturation of the current preamplifier during measurements [29]. For FM-DFM, the microscope is operated in the frequency modulation mode at a small constant oscillation amplitude A_{OSC} of 3.8 Å. Sensor parameters are the unperturbed resonance frequency f_0= 21 kHz, spring constant $k \sim 22\,000$ N m^{-1} and quality factor $Q \sim 25\,000$ of the tuning fork. A Nanosurf

easyPLL[2] has been used as a sensor controller together with a Nanonis system for signal processing and data acquisition[3]. The small amount of postproduction performed on the images consisted of a global levelling, adjustment of the greyscale range and cropping of images [30]. Due to slight thermal drift, the unit cells had to be straightened out. For this purpose, the unit cell of the density functional theory (DFT) model [31] has been taken as a reference. The deviation of the unit cell measures in the model from those experimentally determined by low-energy electron diffraction (LEED) is considered small. The amount of skewing, compressing and/or stretching performed to redimension the unit cells to compensate for deviations from the model adds up to less than 100 pm. The initially mirror-polished (110) surface of a NiAl single crystal is further cleaned in UHV by cycles of sputtering (Ar ions, ∼900 V) and annealing (∼1270 K). Exposure to molecular oxygen in the 10^{-6} mbar range at 550 K and subsequent annealing in vacuum at about 1100 K, each for ∼10 min, produces the ordered oxide film. Holes in the film, if present and not desired, may be closed by repeating the oxidation procedure [32, 33].

3. Translation-related domain boundaries

3.1. Antiphase domain boundaries (APDB) I, II, III and their triple junctions

Most frequent among the APDBs in alumina/NiAl(110) are the domain boundaries labelled types I and II in previous works [33]. These domain boundaries have been described at the atomic level so far [20, 25, 33, 34] and shall be recapitulated before other structures are treated. In figure 1, they can be identified in both reflection domains A and B. In STM empty state images at certain imaging parameters, type I is immediately visible as a straight line parallel to the b_1 direction of the oxide lattice with occasional steps and cascades of steps in the boundary path. This appearance is explained by oxygen-deficient centres in the APDB I unit cell [16, 34, 35]. The straight segments allow direct determination of the domain orientation from microscopy images. Type II appears at the same parameters as a slightly irregular but still rather straight line of round protrusions (pebble chain). The direction of its paths with respect to NiAl[$1\bar{1}0$] also allows determination of domain orientation. Details such as preferred local and global directions, Burgers vectors as well as topographic peculiarities of types I and II have been discussed at length in a previous paper [20]. Basic structures of APDB types I and II are given in the FM-DFM images in figure 2. In figure 3 the characteristics of APDBs I and II are summarized along with those of types III and IV, which will be described in detail later in this paper. Global and local boundary paths are drawn as well as Burgers vectors (drawn to scale) and the average orientations of the quasi-hexagonal Al_S and O_S rows in the oxide surface. The inset shows the Burgers vector orientations with respect to the NiAl(110) substrate.

The central features of alumina/NiAl(110) APDBs are summarized in the following.

- Well-defined ordered structure and hence defined local paths with characteristic structural elements.
- Preferred global directions.
- The formation of arrays with regular spacing (∼9 nm, i.e. $5 \times b_2$) for types I and II.
- Translational displacement with defined Burgers vectors (direction and length) between lattices.

[2] Nanosurf AG, Liestal, Switzerland
[3] SPECS Zurich GmbH, Zurich, Switzerland

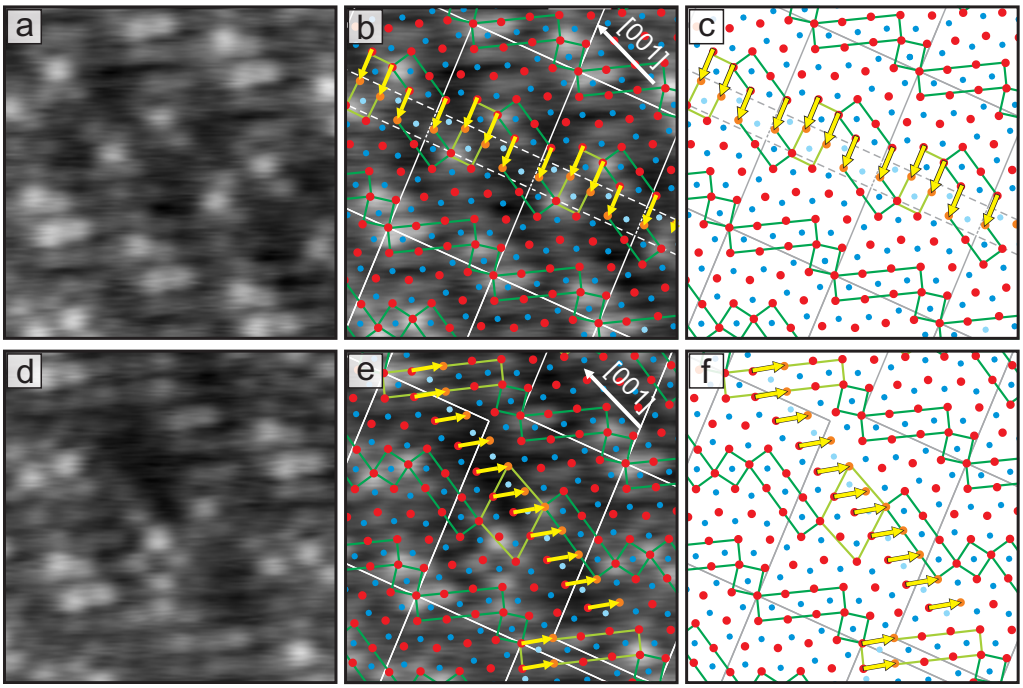

Figure 2. Atomic resolution FM-DFM image of (a) an A I and (d) an A II APDB in alumina/NiAl(110). The images are reproduced in (b) and (e), respectively, covered with Al_S and O_S positions from adjusted DFT models for direct comparison [31]. Panels (c) and (f) give the models without underlying images. Green squares and rectangles indicate the prominent structural building blocks of four and eight oxygen sites with their characteristic topography as well as their altered counterparts (light green) at the APDBs. The contrast in FM-DFM images refers to corrugations of about 50 pm peak to peak. Scan area: 3.1 nm × 3.1 nm. $\Delta f = -3.0$ Hz, $A_{OSC} = 3.8$ Å and $V_S = -200$ mV.

- Burgers vectors along quasi-hexagonal rows of O_S and Al_S sublattices.
- Equal number of atoms introduced into each quasi-hexagonal row.
- Defect structure within APDBs, various building blocks (likely related to glide motion during growth and cooling [15]).
- No obvious lateral strain in the oxide structure surrounding the APDBs.
- Shallow depressions at APDBs I and II. Boundary sites ∼10 pm lower on average.
- Subtle topographic changes in APDBs I, II and IV (possibly induced by local registry).
- Strain relief possible if the Burgers vector has components along NiAl[1$\bar{1}$0].
- Edge and screw character in the underlying dislocations as Burgers vectors $\boldsymbol{b}$ have components not only parallel to the line vector $\boldsymbol{l}$ (boundary path).

As types I and II are known to either cross an entire oxide patch from one RDB, TDB or step edge to another or form junctions between one another, the question arises as to how the observed junctions can grow as flat and regular as they do. With the two Burgers vectors pointing in different directions the junction would cause a problem for the integrity of the oxide

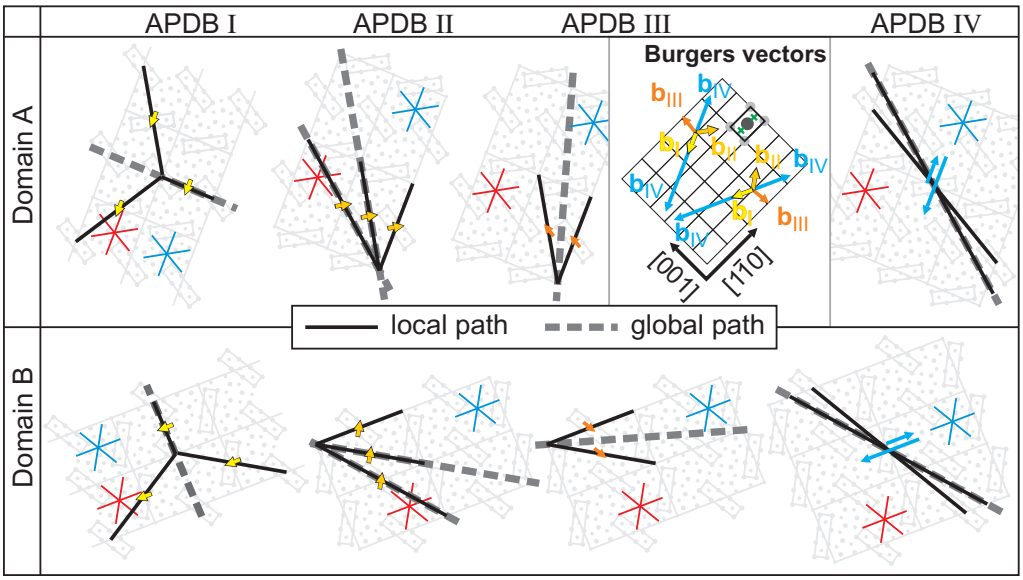

Figure 3. Schemes indicating the orientations of APDB boundaries of types I, II, III and IV in the pristine oxide unit cell for both reflection orientations (A, B). Local (solid black lines) and commonly observed global path directions (dashed grey lines) are indicated. The quasi-hexagonal axes of the O_S and Al_S oxide sublattices (stars of red/blue lines) are plotted alongside the different boundaries. Burgers vectors for the boundaries are shown within each scheme, but also in comparison to the substrate surface lattice (see the inset). The respective Burgers vectors are denoted by the Roman number of the respective boundaries, e.g. $\boldsymbol{b}_{\mathrm{II}}$. Small green crosses on the NiAl unit cell mark two hollow sites 3 Å apart.

on the other side of the connected APDBs I and II. Substantial strain would be the consequence. Therefore, we expected the existence of a third APDB type with appropriate Burgers vector that could prevent this.

The FM-DFM image in figure 4 proves the existence of such a type III APDB. This APDB usually adopts orientations close to the oxide's b_2 direction. Its path, vertical in the figure, is smoother than the discontinuous zigzagged steps of type II, albeit less regular than that of the straight type I. No topographic depression accompanies the boundary in contrast to the previous two types. Together with its different electronic defect signature this could render type III invisible in low-energy electron microscopy (LEEM) images where surface topography, electronic structure and work function affect reflectivity and phase contrast. A bigger problem should be to find an example sufficiently long to enable spatial resolution by LEEM. APDBs III comprise two structural building blocks at different angles towards b_2. As the boundary lengths for type III are typically short and multiples of $2\,b_2$, they are assumed to come in pairs. The generally short length points to an energetical disadvantage of this defect. The latter is probably related to its Burgers vector $\boldsymbol{b}_{\mathrm{III}}$ being nearly perpendicular to the commensurate NiAl[1$\bar{1}$0] direction which does not allow strain relief. As in the cases of APDB I and II, the Burgers vector measures 3 Å. This fact gains importance at the APDB triple junction.

An atomically resolved FM-DFM image of a triple junction $J_{\mathrm{I,II,III}}$ between APDBs of types I, II and III is shown in figure 5 for an A domain. An elbow-shaped depression stemming from

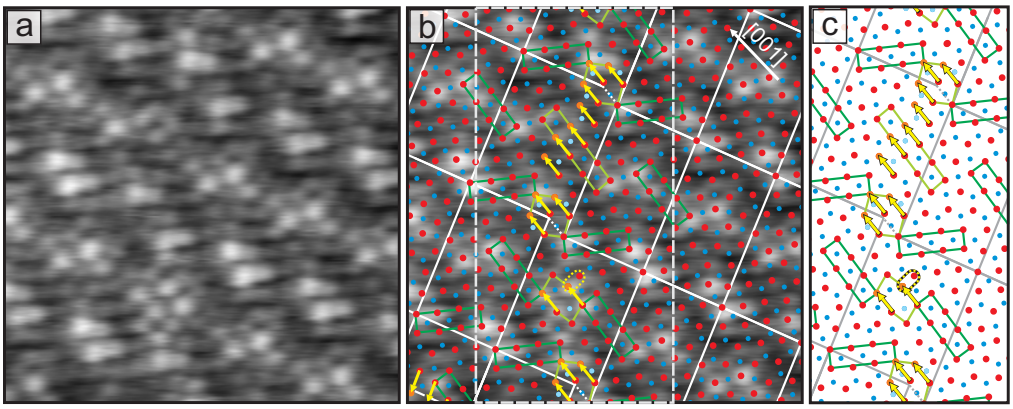

Figure 4. (a) Atomic resolution FM-DFM image of an A III APDB originating from a domain boundary junction (not visible) in the ultrathin alumina/NiAl(110). (b) The same image with an adjusted model superimposed. (c) Model for the area within the dashed white rectangle in (b). Yellow arrows indicate the Burgers vector. Scan area: 5 nm × 5 nm. The cutout measures 5 nm × 2.5 nm. $\Delta f = -2.5$ Hz, $A_{\mathrm{OSC}} = 3.8$ Å and $V_{\mathrm{S}} = -100$ mV.

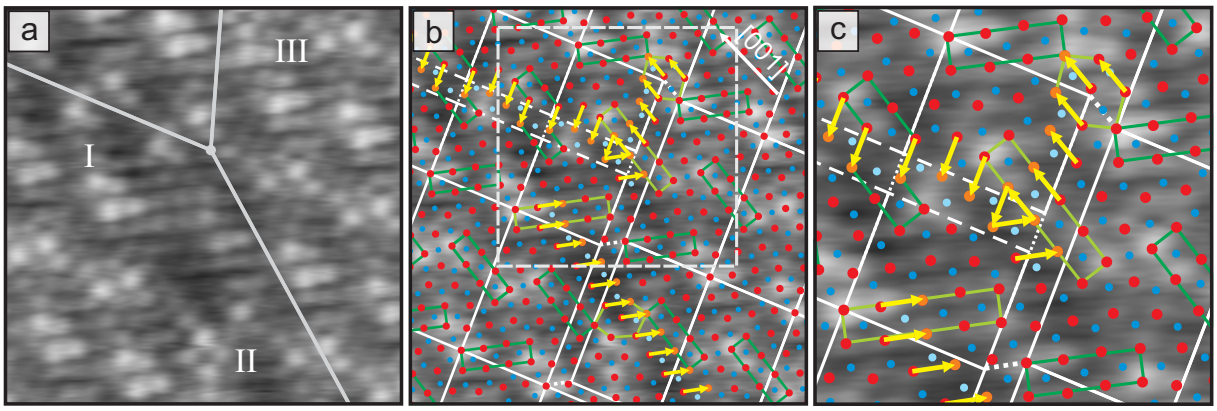

Figure 5. Atomic resolution FM-DFM image of a domain boundary triple junction between boundaries of types A I, A II and A III in the ultrathin alumina/NiAl(110). (b) The same image as in (a) with an adjusted model superimposed [34]. (c) Enlarged cutout from within the dashed square in (b). Yellow arrows indicate the length (3 Å each) and orientation of the Burgers vectors of the three APDBs. Scan area: 4.7 nm × 4.7 nm. $\Delta f = -2.5$ Hz, $A_{\mathrm{OSC}} = 3.8$ Å and $V_{\mathrm{S}} = -100$ mV. Cutout: 2.8 nm × 2.8 nm.

APDBs I and II runs from the top left to the bottom right with the junction slightly above the centre of the image. The junction line with a length equal to the film thickness (5 Å) is parallel to the surface normal. A simplified schematic diagram of the node between the three underlying dislocations at the film–substrate interface has been superimposed onto figure 5(a). The senses of line vectors $\boldsymbol{l}_{\mathrm{I}}, \boldsymbol{l}_{\mathrm{II}}, \boldsymbol{l}_{\mathrm{III}}$ for the defects underlying each boundary are chosen to be away from the node underneath the triple junction. Thus, the Burgers vectors have the orientations indicated in the figure. The unit cell structures of the three individual domains are maintained up to the

three boundaries. This confines the core of the junction between the three APDBs to the very small area of one of the equilateral triangles formed by O_S sites within the oxide unit cell. The triangle may have a character similar to that in the thin alumina film on $Ni_3Al(111)$ where each unit cell comprises such an O_S group with threefold symmetry, special binding and possibly special adsorption properties [23]. No obvious lateral distortions of the atomic structures occur around the boundaries or the junction. Topography shows no changes other than those typical of the three types of APDBs. The junction at the other end of the type III boundary can be expected to equal the structures just presented except for an 180° rotation which is compatible with the twofold symmetry of the oxide structure. The existence of triple junctions now allows the formation of extended networks of APDBs and the associated dislocations. At each junction the Burgers vectors of the three joining APDBs add to zero, thus satisfying Frank's node condition similar to Kirchhoff's law for currents at the junctions in an electric network. If it was not for type III, a displacement in the lattice would result at the junction, which could only be accommodated by straining the O_S and Al_S sublattices, which is not observed. The existence of a closed Burgers vector loop around this line ensures that the junction $J_{I,II,III}$ itself has no dislocation character and explains sufficiently the regular appearance. The existence of APDB III, with its lack of strain relief at the film–substrate interface, is enabled by its prevention of strain build-up at its two terminal junctions. If it is connected to only one or no other APDB, it would have to cross an entire oxide patch or terrace to release the displacement by an appropriate rigid body translation across the encircling step edges, RDBs or TDBs. Such translations in RDBs will be considered later in this paper.

3.2. The defect network

Networks composed of APDBs I, II and III and their triple junctions $J_{I,II,III}$ are frequently observed in the alumina on NiAl(110). The most simple arrangements are arrays of either type I or II APDB crossing a whole oxide patch or even an entire terrace (see figure 1). Other common structures are quite regular mesh patterns. Figure 6(a) shows an STM image of the mesh motif in the domain boundary network of the alumina film. It comprises APDBs of types I and II as well as type III connecting junctions of the previous two. In contrast to the meshes shown here, the pattern can also comprise type I and II segments of similar length, and the type II can adopt the orientation of its intermediate subunit as a global direction. The result is diamond shapes slightly truncated at their tips. Figure 6(b) presents an explanation of the mesh network. It can be understood to originate from two intersecting groups of APDBs: one of type I and another of type II. At each of the junctions the underlying dislocations react and form a fourfold node. The condition $\boldsymbol{b}_I \cdot \boldsymbol{b}_{II} < 0$ for the dislocation reaction in their glide plane (film–substrate interface) is fulfilled. At the node (junction) the sum of all Burgers vectors has to be zero to satisfy Frank's node condition, if lattice strain is to be prevented. This is facilitated by the decomposition of each junction into two triple junctions which are connected by a well-defined segment of APDB III (with underlying dislocation) delivering the required Burgers vector $\boldsymbol{b}_{III}$. The decomposition of a junction between two boundaries into two junctions spanning a segment of a third boundary is known from other domain boundary structures and is explained by the reduction in the overall boundary energy. This picture invokes concepts of stress equilibrium along the boundary planes and the absence of anisotropy for the interfacial free energies of the boundaries. According to these assumptions, the produced nodes would be regular and threefold with 120° angle between the joining boundaries. The deviations in the observed structures (in particular, APDB

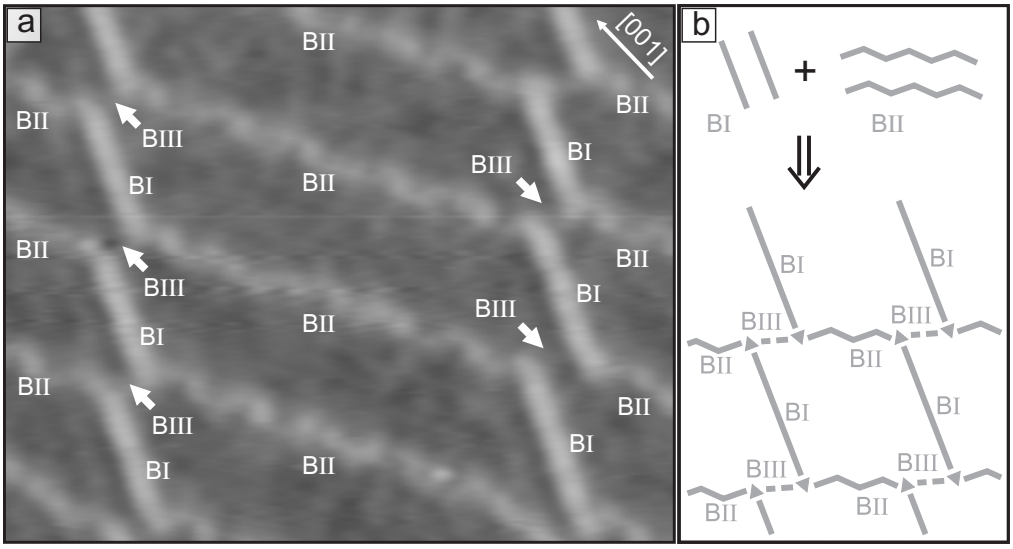

Figure 6. The mesh motif. (a) STM overview of a mesh pattern formed by regular arrangements of strain-relief-related APDBs (types I–III) in alumina/NiAl(110). Scan area 53 nm × 66 nm. $V_S = +5$ V, $I_T = +100$ pA. (b) Diagram illustrating the possible origin of the mesh structures composed of APDBs of types I–III. Two intersecting groups of dislocations underlying the types I and II boundaries react to form fourfold nodes, each of which splits into two threefold nodes, exacting a type III APDB between them.

III produces different angles) are attributed to the anisotropy of the oxide structure and of the epitaxial strain, which impose constraints on the boundary paths. The relations between the APDBs described so far should allow easier and more precise assignment of APDB types in experiments where atomic resolution is not obtained [15, 17].

3.3. APDB type IV

Low-resolution STM images show a fourth type of regular defect in the alumina film. It appears less frequently, but with a unique signature (see the dotted line in the upper right part of figure 1 and on the diagonal of figure 7(d)). It is denoted here by APDB type IV and its translation character as well as its atomic structure are unveiled in the following. It runs in straight lines across whole terraces or oxide patches at an angle of 39° against b_1, sometimes intersecting e.g. type I APDBs. The latter does not involve a third type of boundary in contrast to the triple junctions described above. Figure 7(a) shows an atomically resolved FM-DFM image of a B IV boundary. Large rectangular structures (small arrows) mark the boundary path along the diagonal of the image. They are nearly perpendicular to the wave-like crests of the domains. The misalignment of the wave-like crests on both sides of the boundary identify its translation character. Images recorded at slightly different lateral positions reveal two more such rectangular structures in the upper left and lower right corners of the image. Closer inspection allows the identification of two rectangular groups of six sites sitting nearly opposite each other. In the adjacent unit cells, two blocks of eight O_S sites from the pristine oxide structure of identical orientation face each other, each block belonging to one domain.

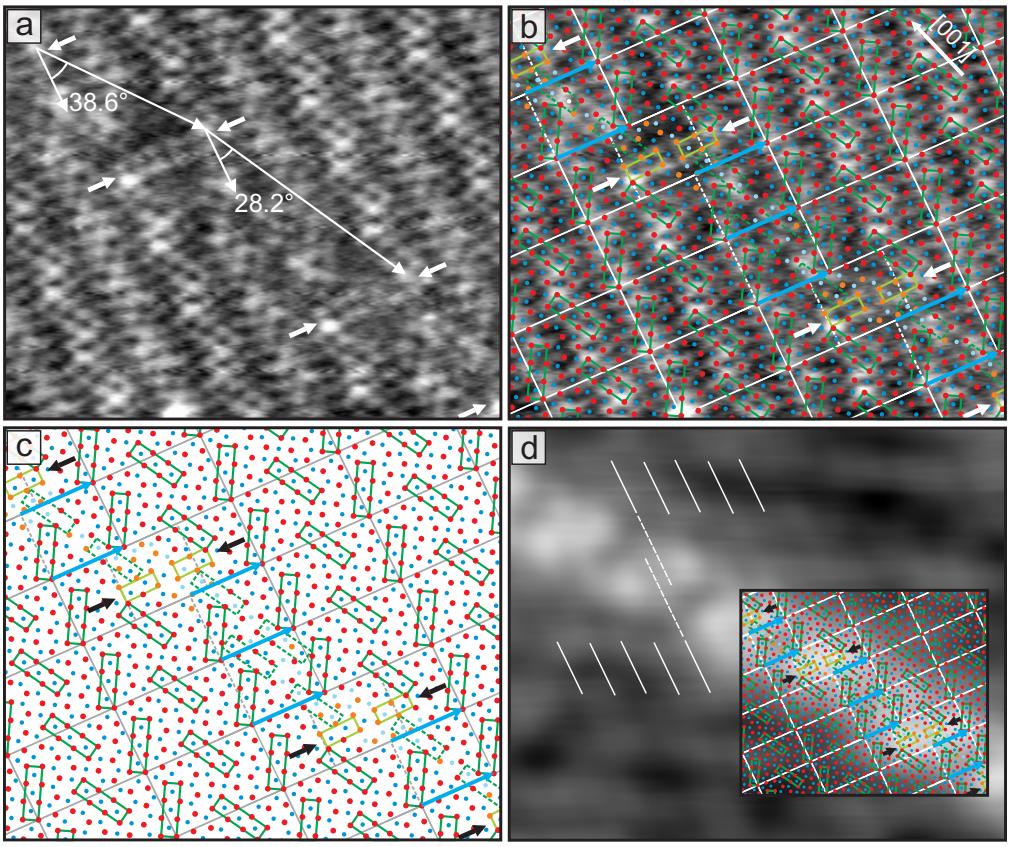

Figure 7. (a) Atomic resolution FM-DFM image of a B IV domain boundary in the ultrathin alumina/NiAl(110). Scan area: 6.3 nm × 7.6 nm; $\Delta f = -7$ Hz, $A_{OSC} = 3.8$ Å and $V_S = -0.5$ mV. (b) The image plus an adjusted model of the O_S and Al_S sublattices. (c) Adjusted model without the underlying image. (d) Model from (b) superimposed on an STM image of the area where (a) has been taken. White lines highlight the faint wave pattern which is associated with the blocks of eight O_S sites. Scan area: 13 nm × 15 nm; $V_S = +3.5$ V and $I_T = +50$ pA.

These two structural building blocks are repeated along the boundary, forming sequences. A short and a long sequence have been found (as indicated in figure 7(a)). They form angles of 38.6° and 28.2° against b_1, respectively. The 39° with respect to b_1 observed at long type IV boundaries suggests that the long segment is rare. This is supported by the underlying STM image in figure 7(d). In figure 7(b) the image has been covered with unit cells from the DFT model and additional positions at the boundary. The resulting model without the underlying image is given in figure 7(c). Only at the boundary O_S sites have been placed differently to cover the observed protrusions. On the atomic scale this boundary produces its own characteristic features as already mentioned above and presented in figures 7(b) and (c) with and without the underlying FM-DFM image. Two blocks of six oxygen sites each connect those crests of the adjacent domains having their structural units (green rectangles) in identical orientation and nearly parallel to NiAl[001]. The new structures arise from the oxygen square within the unit cell model that connect the structural elements to each other. Consequently, the other crest from

each domain does not exist in these cells of the B IV boundary. The emerging structures are spacious, but follow apparently the building rules found for the pristine oxide [23, 31, 34]. The second subunit then suppresses structural elements on the respective other crest, leaving two parallel blocks of eight O_S sites opposite each other. In the space between them, topographic protrusions are reminiscent of the suppressed blocks of the second crest as indicated by dashed rectangles. This is of strongest visibility in the contrast of the short sequence. The second building block at APDB IV is shifted by half a unit cell along b_2 with respect to the first one. It therefore affects the structures on the crest conserved in the first building block. They seem to alternate along the boundary path leading to the electronic states that protrude along APDB IV in zipper-like arrangements of protrusions in empty state STM images (see figure 1). The question arises as to where and how the electronic defects occur which are so typical for this boundary in STM. A direct comparison of the structure observed by FM-DFM with the electronic signature in an STM image, previously recorded at the same position, is shown in figure 7(d). Bright protrusions along type IV boundaries appear in STM at the blocks of $2 \times 6O_S$ sites in the FM-DFM image. They do so at tunnelling parameters comparable to those for detection of the defects introduced by APDBs I and II. This suggests similar kinds of atomic defect structures at the type IV boundary. The faint wave pattern visible in figure 7(d) along b_1 (print reproduction may prohibit this) is closely related to the wave crests produced by the chains of structural elements in the film topography.

The boundary provides a displacement of the oxide lattice only along b_2. But with its 12.1 Å distance between equivalent sites the displacement is several times larger than that of an APDB I or of the other APDBs (3 Å). Taking the rule of thumb for dislocations that defect energy increases proportionally to the square of the Burgers vector [36] to be applicable to the defect network in the ultrathin alumina, such a huge displacement across APDB IV should energetically be very disadvantageous. This, however, conveys another perspective on this boundary. If the picture of impinging oxide patches is adopted, either of the domains lacks only 5.8 Å to the completion of its unit cells. This way, the boundary would imply a favourable translational relation between the two adjacent domains. In both cases the lateral displacements are larger than in the other well-ordered boundaries (APDBs I–III) and probably less energetically favourable. It may be this that forces the boundary to be so well ordered and with hardly any curvature (to reduce defect length) along its path through a domain. This fits the observation that type IV boundaries typically cross whole oxide domains ending at their circumference, i.e. at step edges, RDBs or nucleation-related TDBs. While it cannot be excluded that type IV has its origin in strain relief, we tentatively associate it with the growth from displaced nuclei. The treatment in the context of APDBs and the Roman label are due to the high crystallinity, regular appearance and the fact that type IV usually runs through a domain instead of being part of its perimeter.

3.4. Nucleation-related translation domain boundaries

Nucleation of the alumina structure from the amorphous precursor allows many lateral nuclei spacings that are compatible with translations of the substrate but not the oxide lattice. Simply consider the equivalent substrate sites within the two oxide reflection unit cells in figure 8(a). As each oxide cell covers the area of 16 substrate cells such nucleation-related translation domains are very likely. Their boundaries are generally expected to be the trivial case in domain boundary formation during growth if the epilayer unit cell is larger than that of the substrate. However,

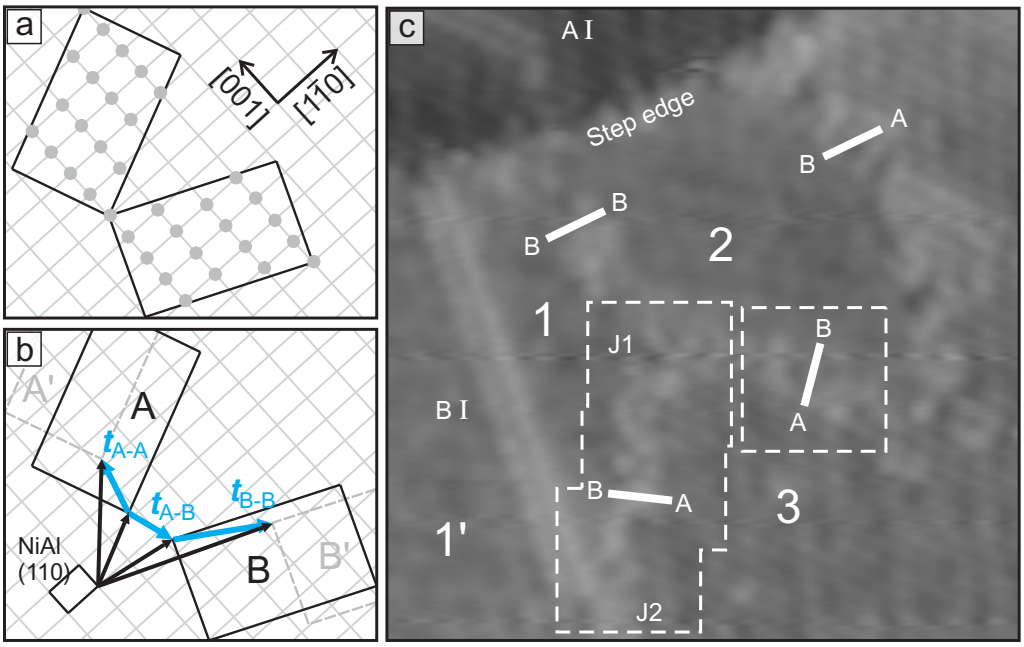

Figure 8. (a) Sketch of the numerous substrate sites (grey circles) for which incompatible translational relations result if the lattices of two oxide domains do not originate from only one of them. The scheme is drawn for the DFT model, but is qualitatively identical for the unit cell measures from LEED. (b) Translation vectors between nucleation-related translation domains and reflection domains. (c) STM overview image of the area where images in figures 10 and 11 have been recorded at the positions marked by dashed boxes. Boundaries are labelled with either their APDB symbols or letters giving the reflection orientation of each of two adjacent domains. J1 and J2 mark domain boundary junctions and large Arabic numbers label the surrounding domains. Scan area: 31 nm × 31 nm; $V_S = +3.5$ mV and $I_T = +250$ pA.

the boundaries do not have to be abundant. Their number decreases with annealing time and temperature, i.e. they are rare, probably of little order, and due to the rich number of possible translation relations at low occurrence, hard to investigate. To the authors' knowledge they have not been shown before for alumina/NiAl(110). The understanding of translation vectors ($\boldsymbol{t}_{A-B}$, $\boldsymbol{t}_{B-A}$, $\boldsymbol{t}_{A-A}$, $\boldsymbol{t}_{B-B}$) between two nucleation-related translation domains with or without additional reflection is depicted in figure 8(b) as the difference vector between position vectors of equivalent oxide lattice sites. For the cases A–A and B–B they are easily determined to be the smallest possible spacing between equivalent O_S sites across the domain boundary or, on the contrary, the distance lacking to the completion of the interrupted unit cell. The situation is more involved for reflection domains. In figure 8(c), several oxide domains with different translation and reflection relations and the boundaries between them are displayed. Near the middle of the image a triple junction, denoted by J1, is formed by two RDBs (B–A, A–B) and the previously mentioned nucleation-related TDB (B–B). Its translation nature will be proven and the displacement will be shown to measure $\boldsymbol{t}_{B-B} = 14.2$ Å (see figure 10). In the lower left part of the image, the junction J2 between one RDB and an APDB I is located. The domains

forming these boundaries and junctions have been labelled 1′, 1, 2 and 3. Atomically resolved FM-DFM images of the boundaries and the adjacent junctions are given in figures 10 and 11. The respective scan areas are marked with dashed boxes in figure 8(c). While it may be assumed that certain advantageous translation relations can lead to TDBs of the types presented above (especially IV), the more general case is presented at the atomic level in the following section together with RDBs.

4. Reflection domain boundaries

A RDB is formed where domains with different mirror orientations meet. In alumina/NiAl(110) the two mirror or reflection orientations (A, B) are induced by the reduced point symmetry with respect to the substrate. Epitaxy defines the required mirror plane, spanned by the surface normal vector and the NiAl[1$\bar{1}$0] axis, a common surface normal for all domains in the film and the rotation of both lattices against the mirror plane about the surface normal by $\pm 24^\circ$. The relative orientation of the lattices (angle–axis pair; mirror plane) is thus always the same: $2 \times 24^\circ$, [$\bar{1}\bar{1}$0]; (001). Only the inclination of the boundary path against NiAl[1$\bar{1}$0] and the boundary position vary. Therefore individual RDBs can simply be compared by their angles towards b_2 of one of the adjacent domains (or NiAl[1$\bar{1}$0], respectively) and the relative translation of the two adjacent lattices. The RDBs constitute a quasi-2D version of reflection boundaries in bulk crystals.

Several aspects contribute to the orientation and position and hence to the structure of a boundary. Besides minimization of elastic strain as well as the interface area and energy, the lattice misorientation and mutual translation may affect the structure by enforcing certain path directions. Symmetric RDBs which run parallel to NiAl[1$\bar{1}$0] [37] could form directly during growth, being possibly only slightly less favourable energetically than the bare domain, as their creation may require comparably small changes in bond lengths or angles when the RDB runs parallel to the mirror plane. This would be the quasi-2D correspondence to growth reflection twins in bulk crystals. However, this idea does not include the rather complex basis of the oxide unit cell and lack of a mirror plane coplanar to that of the substrate therein. The observed RDBs are more often asymmetric as they most likely constitute boundaries between impinging domains originating from different nuclei. Such nuclei can have the same arbitrary translational relation as previously described for nucleation-related TDBs. RDBs are usually observed to encircle reflection domains together with a segment of a terrace step edge or a nucleation-related TDB. Their boundary planes can have multiple inclinations with respect to a chosen oxide or substrate lattice direction. Consequently, they tend to be of lower order and irregular line shape on the larger scale. Nevertheless, close to symmetric RDBs have occasionally been observed and paths can sometimes be approximated by a sequence of lines with different inclinations where some orientations seem preferred [37, 38].

In order to analyse this and to develop a structural model, the *dichromatic pattern* and *coincidence site lattice* (CSL) approach has been pursued [39]. A dichromatic pattern in general is formed by two interpenetrating crystal lattices and for alumina/NiAl(110) in particular it is the superposition of the lattices for domains A and B. Each lattice gets arbitrarily assigned a colour for identification. A CSL is the set of points which belong to both lattices. Actual structures are obtained by identification of the boundary region, attachment of the two bases on the respective sides of it and placement of alternative or additional atom positions at the boundary if necessary. This approach seems suitable for the present case of a high-angle domain

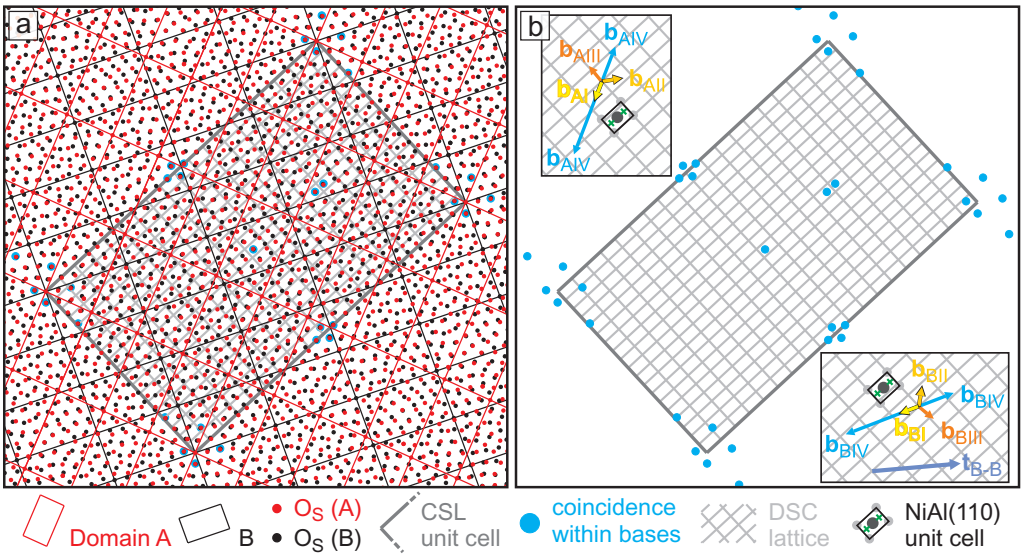

Figure 9. (a) CSL unit cell (bold grey lines) within the dichromatic pattern of the two alumina/NiAl(110) reflection domains A (red) and B (black). Bases (here only O_S sites) are already attached to the dichromatic pattern. Component lattice dimensions: $b_1 = 10.55$ Å, $b_2 = 17.88$ Å, $\alpha = 88.7°$, mutual rotation: $\pm 24.07°$, fractional coordinates from the DFT model [31]. Blue circles highlight sites where (in-)equivalent positions in the respective bases coincide. Translations of one of the lattices against the other on the fine lattice (DSC lattice) within the CSL unit cell conserve both, the CSL and dichromatic pattern. (b) CSL unit cell with DSC lattice from (a) and Burgers vectors of the TDB and APDBs presented earlier in the text drawn to scale onto enlarged sections of the DSC lattice. Black rectangles for single NiAl(110) unit cells (2.89 Å × 4.08 Å) have been drawn onto the light grey DSC lattices (2.4 Å × 4.1 Å) in the insets in (b) for direct comparison.

boundary (misorientation angle >15°) where an analysis in terms of dislocation arrays becomes impossible. The following points have been noted.

(i) Two lattices with the LEED dimensions for the alumina/NiAl(110) are supposed to form a CSL at an angle of $2 \times 24.07°$ towards each other. This is very close to the $2 \times 24°$ from the LEED study and according to the Brandon criterion[4] fulfils the requirements for coincidence [41][5]. Therefore a 2D CSL exists within experimental uncertainty and measures 46 Å × 78 Å (see figure 9(a)).

(ii) The CSL and oxide unit cells have an area ratio of $\Sigma = 19$, i.e. of low-sigma type, which often implies beneficial boundary properties such as low interface energies [42].

(iii) With the slightly broadened cell from the DFT model, no such CSL is found.

[4] $\Delta\Theta = \Theta_0/\sqrt[n]{\Sigma}$ [40].

[5] The Brandon criterion gives the maximum permittable deviation angle from ideal coincidence orientation based on a maximum angular value Θ_0 for low-angle boundaries (usually taken to be 15°) and a superimposed subboundary network on the CSL that is limited by the density of CSL points, i.e. by Σ. Brandon suggested $n = 0.5$, but values up to unity have been proposed and may be more suitable for certain purposes.

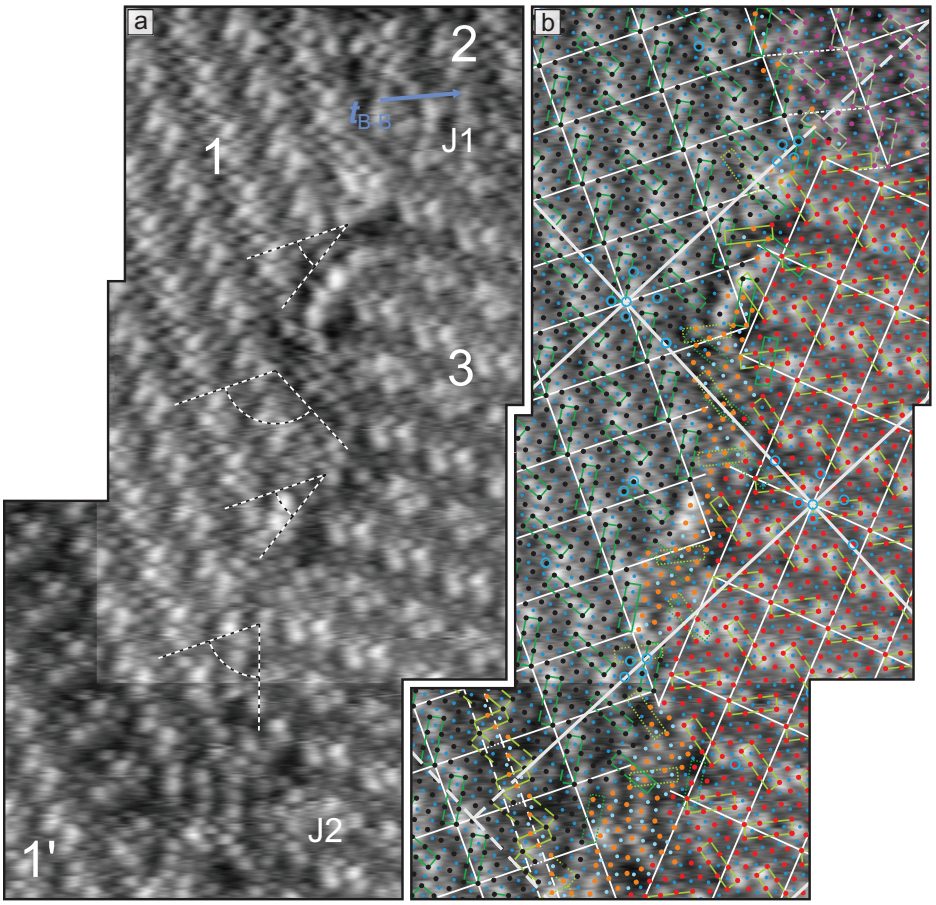

Figure 10. (a) Composite of three atomically resolved 6.7 nm × 6.7 nm FM-DFM images of RDBs and their junctions (J1, J2) with a nucleation-related TDB as well as with an APDB B I. The images have been recorded inside the large dashed box in figure 8. Local orientations of the boundary path with respect to b_2 are indicated. (b) The same composite covered with a model derived from a dichromatic pattern based on LEED lattice parameters and DFT fractional coordinates. Blue circles mark sites where (in-)equivalent red and black O_S sites are not more than 20 pm apart in the dichromatic pattern. The CSL unit cells are drawn in grey between J1 and J2. Overall size: 8.7 nm × 15 nm. $\Delta f = -1.7$ Hz, $A_{OSC} = 3.8$ Å and $V_S = -250$ mV.

(iv) In connection with the CSL there exists a lattice of *displacements which are symmetry conserving* (DSC lattice). Its rectangular unit cell measures 2.4 Å × 4.1 Å. Close inspection of the insets in figure 9(b) reveals that it equals the NiAl(110) unit cell (black rectangles: 2.89 Å × 4.08 Å) in length, but not in width.

(v) RDBs with boundary paths beyond those given by low-index CSL lines exist and seem to be even more abundant.

(vi) Attachment of the bases lowers the symmetry of the dichromatic pattern as it destroys the twofold rotation axis.

(vii) None of the APDB or TDB displacements is a DSC lattice translation (figure 9(b)).

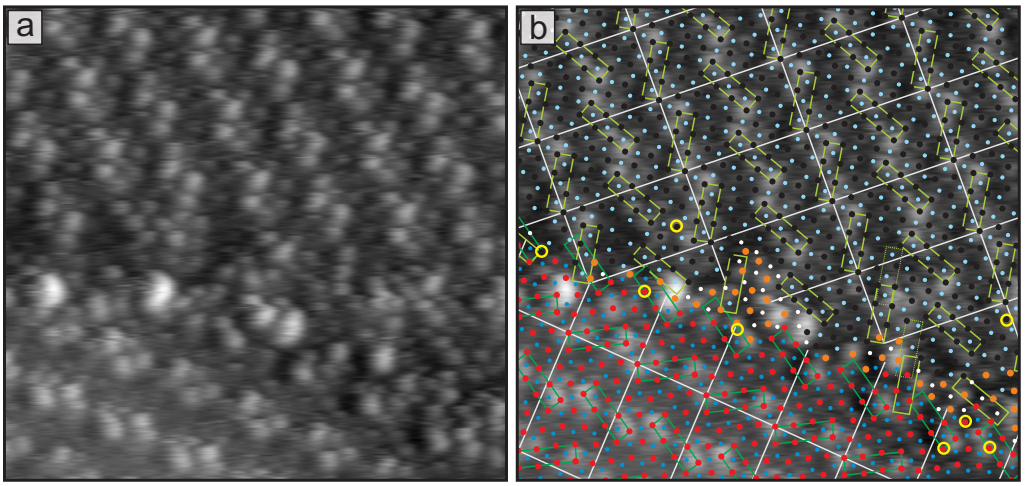

Figure 11. (a) Atomic resolution FM-DFM image of the RDB taken within the square box in figure 8. Scan size: 6.6 nm × 7 nm, $\Delta f = -1.6$ Hz, $A_{OSC} =$ 3.8 Å and $V_S = -250$ mV. (b) The same image as in (a) but with a model superimposed. The model has been generated from a dichromatic pattern. Places where (in-)equivalent red and black O_S sites in the dichromatic pattern are not more than 20 pm apart are indicated by yellow circles.

The dichromatic pattern shown constitutes the high-symmetry form without any rigid body translations, but already the attachment of the bases to the red and black lattices reduces the symmetry. New coincidence sites appear (marked with blue circles) not more than 20 pm apart. Some of them mark the coincidence between inequivalent positions within the red and the black basis. This will affect the selection of possible RDB structures just as rigid body translations will affect symmetry and structure.

The presence of a CSL and its DSC lattice is fortunate as epitaxy is determined primarily by the interaction between the oxide domain and the substrate and not by favourable relations between abutting oxide domains. The CSL gives an unambiguous starting point for image analysis and, to some extent, insight into lattice translations even across RDBs. This is enabled by its DSC lattice. Any relative translation between abutting A and B domains consistent with the DSC lattice conserves not only the CSL, but also the complete dichromatic pattern including the DSC lattice. Together they get shifted laterally. The direction and magnitude of this shift can differ substantially from that of the DSC translation. Only translations within the DSC unit cell alter the dichromatic pattern. Therefore the total vector of any relative translation separates into a conserving part associated with a shift of the boundary path and a non-conserving part which changes the dichromatic pattern as well. Translation vectors within the DSC cell presumably bring about entirely different boundary paths and structures. In turn such translations may be determined from the dichromatic pattern and its DSC lattice. DSC translations between two sections on one side of an RDB produce dislocations on the DSC lattice, the so-called secondary dislocations, which are known to produce step-like faceting of the boundary path. Nevertheless, despite a potentially favourable $\Sigma = 19$ orientation, the expected benefit, namely the existence of points of good contact between the two lattices at the CSL points, is counteracted by the huge extension of the CSL compared to atomic structures within the bases. While alumina/NiAl(110) RDBs following low-index directions of the CSL

have indeed been observed (compare e.g. figure 4.20 in [38] with figure 9(a)), they seem outnumbered by asymmetric non-CSL boundaries.

Turning to the FM-DFM image in figure 10(a), the first atomically resolved image of an RDB in alumina/NiAl(110), and placing the lattices in the arrangement of figure 9(a) one easily finds a good match for the area between junctions J1 and J2. However, this match does not extend across the whole image. Rigid body translations have to be introduced between domains 1′ and 1 as well as between domains 1 and 2 due to the B I and the B–B TDB to place the model correctly (figure 10(b)). The 3 Å displacement across B I APDB and the 14.2 Å displacement at B–B TDB are at the same time the rigid body translations of domains 1′ and 2 towards domain 3. It is found that the introduced shifts are not translations on the DSC lattice and are confirmed by changes of the dichromatic pattern (that is why coincidence of (in-)equivalent red and black O_S sites is marked by yellow instead of blue circles in figure 11(b)). From figure 9(b) it becomes clear that none of the previously described TDBs complies with the DSC lattice translations. Hence, they do not simply produce secondary dislocations at the RDBs, which is the most probable reason for the broad disordered area, e.g. at junction J2 in figure 10. Therefore the integration of TDB displacements at RDBs does not seem advantageous but is probably enabled by energy gain elsewhere, e.g. during alumina/NiAl(110) interface formation and epitaxial strain relief. This possibility should be limited, which could explain the frequently observed continuation of an A(B) IV APDB by a B(A) I APDB across an RDB (see e.g. figure 1).

Considering that the average direction of the A-B RDB in figure 10 has roughly (11) orientation in the CSL, but with at most two CSL points on this boundary segment, the question arises as to what else has an impact on the boundary structures. It could be that the nearby junction J1 puts constraints on the boundary path even though it is close to equilibrium itself. In that case the boundaries meeting at a triple junction line ought to form angles of 120° if no anisotropies in interface energies are present. With angles close to 120°, junction J1 represents such a case. Once the APDB gets involved, at junction J2, the situation changes as in the case of the APDB junction $J_{I,II,III}$.

A closer look at the structures in the images yields the following. The boundary segment between J1 and J2 forms facets along certain directions. Two strips run nearly parallel to the long edge of the CSL unit cell, i.e. to NiAl[1$\bar{1}$0]. While there are no repeated structures along the RDB, sections with sites protruding significantly higher from the oxide domain alternate with areas of rather low and flat topography. The flat areas at the RDB seem to coincide with positions in the dichromatic pattern where the reflection domains connect via their O_S blocks that are parallel to NiAl[001]. This points again towards a strong influence of the oxide bases and their symmetry onto the boundary and seems to support arguments for symmetry-related extensions of the CSL scheme [43]. Another interesting aspect of these alumina RDBs is the orientation of the quasi-hexagonal O_S and Al_S sublattices. If their deviation from hexagonal structure is neglected, RDBs constitute low-angle rotation boundaries of $\sim$12°.

While RDB inclinations along CSL vectors may lead to preferred large-scale boundary paths it should be the basis that determines the structure at the length scale of a unit cell. Experience with the influence of the quasi-hexagonal structures in the unit cell on APDBs I and II supports this. However, a comprehensive treatment of the boundary structure according to the full theory of grain boundaries is beyond the scope of this work [39, 44]. One limiting factor is the large CSL, the large and complex oxide basis and the small DSC lattice cell. If partial dislocations on the latter lattice played a role, this would be difficult to detect. Considering the atomic structure in figures 10 and 11, which has been recorded within the dashed boxes in

figure 8, showing the A–B/B–A RDBs between domains 1, 2 and 3, it is noticed that no random holes need to occur at the RDBs of the alumina film, a question that has previously only been addressed by carbon monoxide desorption or spectroscopy experiments [25, 45]. One further notices that the structural deviations from the usual film topography and structure are confined to a strip that is only slightly wider than 1 nm, i.e. unit cell dimensions. The few larger protrusions along the RDB segments in figures 10 and 11 have some resemblance to the protrusion in the image series of figure 7 (see the bottom of that image). Typically they are only 50 pm higher than the topmost O_S sites. Being too small for a weakly bound larger adsorbate, they may represent hydroxyls. While the film is, in general, quite inert against hydroxylation, it could be possible that a few such sites are provided at the boundaries. As the observed O_S contrast in the FM-DFM images shows sites with higher electron density, there is a possibility that the protrusions are produced by point defects. While STM studies did not find point defects within alumina domains, the boundaries have been shown to exhibit such defect centres [34]. Such defects could also contribute to the electronic signature of RDBs. Eventually the protruding features could refer to dislocations within the quasi-hexagonal sublattice.

5. Conclusions

In conclusion, atomically resolved frequency modulation dynamic force microscopy images have been employed to study the defect network of the ultrathin alumina grown on NiAl(110). The defects arise where domain boundaries of the film penetrate its surface. APDBs originating from strain relief, nucleation-related TDBs and RDBs as well as three types of domain boundary junctions have been resolved, and models for their surface atomic layers have been assigned. Previously neglected boundary types had to be included to develop a consistent picture of, for example, the mesh motif within the domain boundary (the so-called line defect) network. The Burgers vectors of the APDBs allow the formation of triple junction lines free of any dislocation character throughout the mesh network where such junctions play an essential role. Furthermore, clear evidence has been found for arbitrary translations between domains which originated from different nucleation sites. This can be detected irrespective of their reflection symmetry. RDBs have been found to be based on a predicted $\Sigma = 19$ relation between the adjacent lattices, which may be considered a low-sigma orientation typically associated with special physical boundary properties. However, due to the large and complex alumina bases the CSL approach alone does not suffice to bring about a description of orientations or positions of boundary paths and their structures. This becomes obvious from the shown asymmetric RDBs.

With this substantially extended description of the domain boundary network in the alumina film on NiAl(110), future determination of their nature in SPM and LEEM images will be easier and more precise. The very same structures observed here may be expected to occur in the closely related aluminium oxide structures on surfaces where d-metals are alloyed with aluminium. Except that different substrate structures or symmetries suppress certain types of boundaries, e.g. APDBs, or introduce different types such as rotation-related boundaries.

In general, the results of this study should enable improved employment of the alumina/NiAl(110) model catalyst support with much lower uncertainty regarding the domain boundaries and their structure. This is a prerequisite for high-resolution studies on individual adsorbates whose electronic and vibronic behaviour may vary from site to site.

Acknowledgments

We are indebted to Hans-Peter Rust and Gero Thielsch for assistance with the experimental setup.

References

[1] Randle V 2010 *Mater. Sci. Technol.* **26** 253
[2] Hilgenkamp H and Mannhart J 2002 *Rev. Mod. Phys.* **74** 485
[3] Freund H-J 1999 *Faraday Discuss.* **114** 1
[4] Franchy R 2000 *Surf. Sci. Rep.* **38** 195–294
[5] Libuda J and Freund H-J 2005 *Surf. Sci. Rep.* **57** 157
[6] Kulawik M, Nilius N and Freund H-J 2006 *Phys. Rev. Lett.* **96** 036103
[7] Nilius N, Ganduglia-Pirovano M V, Brázdová V, Kulawik M, Sauer J and Freund H-J 2008 *Phys. Rev. Lett.* **100** 096802
[8] Desikusumastuti A, Laurin M, Happel M, Qin Z-H, Shaikhutdinov S and Libuda J 2008 *Catal. Lett.* **121** 311
[9] Sobota M, Nikiforidis I, Hieringer W, Paape N, Happel M, Steinrück H-P, Görling A, Wasserscheid P, Laurin M and Libuda J 2010 *Langmuir* **26** 7199
[10] Heinrich A J, Gupta J A, Lutz C P and Eigler D M 2004 *Science* **306** 466
[11] Qiu X H, Nazin G V and Ho W 2003 *Science* **299** 542
[12] Qiu X H, Nazin G V and Ho W 2004 *Phys. Rev. Lett.* **92** 206102
[13] Bäumer M and Freund H-J 1999 *Prog. Surf. Sci.* **61** 127
[14] Schauermann S, Johánek V, Laurin M, Libuda J and Freund H-J 2003 *Chem. Phys. Lett.* **381** 298
[15] McCarty K F, Pierce J P and Carter B 2006 *Appl. Phys. Lett.* **88** 141902
[16] Heinke L, Lichtenstein L, Simon G H, König T, Heyde M and Freund H-J 2010 *Chem. Phys. Chem.* **11** 2085
[17] Chen Zh. W, Fujita S and Fukui K-I 2011 *J. Phys. Chem.* C **115** 14270
[18] Prévot G, Naitabdi A, Bernard R and Borensztein Y 2010 *Phys. Rev.* B **81** 085405
[19] Burkardt S and Erbudak M 2010 *Phys. Rev.* B **81** 085417
[20] Simon G H, König T, Rust H-P, Heyde M and Freund H-J 2009 *New J. Phys.* **11** 093009
[21] Vizzini S, Oughaddou H, Hoarau J Y, Bibérian J P and Aufray B 2009 *Appl. Phys. Lett.* **95** 173111
[22] Napetschnig E, Schmid M and Varga P 2008 *Surf. Sci.* **602** 1750
[23] Schmid M, Kresse G, Buchsbaum A, Napetschnig E, Gritschneder S, Reichling M and Varga P 2007 *Phys. Rev. Lett.* **99** 196104
[24] Kizilkaya O, Hite D A, Zehner D M and Sprunger P T 2003 *Surf. Sci.* **529** 223
[25] Libuda J, Winkelmann F, Bäumer M, Freund H-J, Bertrams Th., Neddermeyer H and Müller K 1994 *Surf. Sci.* **318** 61
[26] Rust H-P, Heyde M and Freund H-J 2006 *Rev. Sci. Instrum.* **77** 043710
[27] Heyde M, Sterrer M, Rust H-P and Freund H-J 2005 *Appl. Phys. Lett.* **87** 083104
[28] Heyde M, Simon G H, Rust H-P and Freund H-J 2006 *Appl. Phys. Lett.* **89** 263107
[29] Olesen L, Brandbyge M, Sørensen M R, Jacobsen K W, Lægsgaard E, Stensgaard I and Besenbacher F 1996 *Phys. Rev. Lett.* **76** 1485
[30] Horcas I, Fernández R, Gómez-Rodríguez J M and Colchero J 2007 *Rev. Sci. Instrum.* **78** 013705
[31] Kresse G, Schmid M, Napetschnig E, Shishkin M, Köhler L and Varga P 2005 *Science* **308** 1440
[32] Jaeger R M, Kuhlenbeck H, Freund H-J, Wuttig M, Hoffmann W, Franchy R and Ibach H 1991 *Surf. Sci.* **259** 235
[33] Kulawik M, Nilius N, Rust H-P and Freund H-J 2003 *Phys. Rev. Lett.* **91** 256101
[34] Schmid M, Shishkin M, Kresse G, Napetschnig E, Varga P, Kulawik M, Nilius N, Rust H-P and Freund H-J 2006 *Phys. Rev. Lett.* **97** 046101
[35] Nilius N, Kulawik M, Rust H-P and Freund H-J 2004 *Phys. Rev.* B **69** 121401

[36] Haasen P 1970 Dislocations *Physical Chemistry—An Advanced Treatise* vol X ed H Eyring, D Henderson and W Jost (New York: Academic) chapter 2, pp 69–150
[37] Højrup Hansen K, Worren T, Lægsgaard E, Besenbacher F and Stensgaard I 2001 *Surf. Sci.* **475** 96
[38] Heemeier M 2005 *PhD Thesis* Freie Universität Berlin
[39] Sutton A P and Balluffi R W 1995 Interfaces in crystalline materials *Monographs on the Physics and Chemistry of Materials* (Oxford: Clarendon)
[40] Brandon D G 1966 *Acta Metall.* **14** 1479
[41] King A H and Shekhar S 2006 *J. Mater. Sci.* **41** 7675
[42] Miura H, Kato M and Mori T 1990 *J. Phys. Colloq.* **51** C1–263
[43] Bendersky L A and Cahn J W 2006 *J. Mater. Sci.* **41** 7683
[44] Bollmann W 1970 *Crystal Defects and Crystalline Interfaces* (Berlin: Spinger)
[45] Winkelmann F, Wohlrab S, Libuda J, Bäumer M, Cappus D, Menges M, Al-Shamery K, Kuhlenbeck H and Freund H-J 1994 *Surf. Sci.* **307–309** 1148